Boundary-Layer Meteorology (2025) 191:4
https://doi.org/10.1007/s10546-024-00894-6

RESEARCH ARTICLE

Linkage Between Vertical Coupling and Storage Flux: Insights from Urban Tall-Tower Eddy Covariance Measurement

Changxing Lan[1] · Christopher Claus Holst[1] · Thomas Grünwald[2] · Matthias Mauder[1,2]

Received: 13 March 2024 / Accepted: 17 December 2024

Abstract
The storage flux, corresponding to disequilibrium between observed flux and net surface emissions, poses a significant source of uncertainty in tower-based eddy covariance (EC) measurements over urban and forest ecosystems. In this study, we investigated the coupling between the urban inertial sub-layer (ISL) and roughness sub-layer (RSL) and its influence on nighttime storage flux, leveraging tower-EC together with collocated wind profile measurements. Our findings demonstrate that substantial storage flux occurs when the gradient of turbulent kinetic energy (TKE) enlarges, indicating decoupling between ISL and RSL. With increasing wind speed, turbulent eddies generated by bulk wind shear directly interact with the surface, conducive to the recoupling between ISL and RSL and resulting in decreased storage flux. Conversely, when the gradient of TKE between ISL and RSL is small, the storage flux remains low and relatively insensitive to wind speed. The derived diagnostic relation further confirms the predominant influence of stability and turbulent intensity gradient on regulating the storage flux. These results provide valuable insights as a complement to prior storage flux studies in the context of canopy flow.

Keywords Eddy covariance · Storage flux · Vertical coupling

1 Introduction

With the recognition of global warming driven by anthropogenic greenhouse gas emissions, the development of climate action plans has propelled urban eddy covariance (EC) measurements to directly monitor the exchange of (CO_2) between the land surface and atmosphere (Crawford and Christen 2014; Schmutz et al. 2016; Davis et al. 2017; Roth et al. 2017; Lin et al. 2018; Stagakis et al. 2019; Matthews and Schume 2022; Ward et al. 2013, 2022). Despite the advantage of urban EC measurements in describing temporal-spatial patterns in net (CO_2) emissions, challenges arise in hands-on data interpretation, particularly when utilizing tall-tower EC fluxes to improve quantification and understanding of urban (CO_2) emissions. These challenges are primarily related to the inherent heterogeneity of urban environments, which

✉ Changxing Lan
changxing.lan@kit.edu

1 Karlsruhe Institute of Technology, IMK-IFU, 82467 Garmisch-Partenkirchen, Germany

2 Institute of Hydrology and Meteorology, Dresden University of Technology, 01737 Tharandt, Germany

Published online: 08 January 2025

represent non-ideal measurement conditions, violating the basic assumptions of the EC technique (e.g., steady-state conditions, (Mauder et al. 2021)). The non-ideal conditions for urban tower-EC measurements are not only represented by the heterogeneous distribution of (CO_2) sources/sinks (Schmutz and Vogt 2019) but are also manifested in the form of multi-layer structures of the urban surface layer (Oke et al. 2017). The complexity of urban landscapes necessitates that urban tower-EC measurements be conducted in the inertial sub-layer (ISL) to ensure that resultant fluxes are representative of a neighborhood scale, relatively constant with height, and exhibit minimal variation within the fetch, thereby ensuring meaningful and cross-comparable results (Grimmond and Ward 2021).

The tall-tower EC with measurement heights of around 100 m, indeed, reaches the ISL in many cases and provides sufficiently large fetch areas to capture exchanges for a relevant urban area; however, the substantial air volume in the urban canopy layer beneath the measurement height may introduce significant disequilibrium between the observed vertical turbulent exchange and the surface net fluxes. This disequilibrium, referred to as storage flux, is a term in the conservation of the mixing ratio equation that relates to the accumulation or depletion of a scalar (e.g., (CO_2)) in an imaginary control of volume centered at the EC flux tower (Montagnani et al. 2018). In the context of tall-tower measurements above the canopy, it is attributed to the decoupling between the ISL and the underlying roughness sublayer (RSL), resulting from enhanced atmospheric stability and suppressed turbulence (Mahrt et al. 2018). In such a scenario, turbulent eddies become detached from the surface, losing their immediate connection to the exchange of (CO_2), thereby leading to a positive (CO_2) storage flux (Jocher et al. 2018, 2020; Peltola et al. 2021; Stiegler et al. 2023). Additionally, topographical variation may induce horizontal advection within the RSL, exchanging (CO_2) with areas outside the EC footprint, resulting in vertical variability of (CO_2) flux (Feigenwinter et al. 2008, 2010; Siebicke et al. 2012). The Hockey-Stick Transition (HOST) hypothesis is proposed to explain the generation of large coherent eddies and their contribution to vertical variations in turbulent intensity and atmospheric stratification (Sun et al. 2012, 2016). Therefore, the linkage between turbulent transport and the vertical coupling state of the atmospheric boundary layer can be established. A series of studies have investigated the vertical coupling state by examining the correlation between turbulent intensity above and below the forest canopy (Acevedo et al. 2009; Thomas et al. 2013; Jocher et al. 2018, 2020; Freundorfer et al. 2019). While the thresholds are site-dependent, these studies consistently reveal that wind speed is an indicator for classifying the vertical coupling state. Under strong wind conditions, the linear relationship of turbulent intensity above and within the canopy provides evidence for full vertical coupling. In weak wind conditions, on the contrary, the turbulent intensity above the forest canopy is independent of that within the canopy, indicative of vertical decoupling. During such vertically decoupled regimes, (CO_2) accumulates within the forest canopy due to limited vertical transport, implying that (CO_2) flux measured above the canopy likely underestimates the surface (CO_2) flux due to the corresponding flux difference. The accumulated (CO_2) can be transported to the measurement height above the canopy during consecutive strong wind conditions, together with intermittent turbulence, partially compensating for the preceding underestimation (Oliveira et al. 2018; Freundorfer et al. 2019). Nevertheless, the venting of (CO_2) attributed to horizontal advection during the decoupled periods results in a misestimation of the (CO_2) flux (Jocher et al. 2018). Hence, a (CO_2) flux filtering approach in terms of coupling state is crucial to derive adequate estimates of net ecosystem exchange and accumulated carbon for forest ecosystems (Jocher et al. 2018, 2020).

The storage flux has long been recognized as a source of uncertainty in tower-EC measurements, and effort has been devoted to understanding its relation to the vertical coupling state

over ecosystems. However, due to the logistical challenge in deploying profile measurements over urban areas, relatively little attention has been paid to exploring the vertical coupling state and its influence on storage flux in urban environments, which is nevertheless necessary (Lietzke and Vogt 2013; Crawford and Christen 2014). In this study, we aim to (i) advance the mechanistic understanding of how the coupling between ISL and RSL influences the storage flux and (ii) propose a diagnostic relation for the storage flux.

2 Instrumentation, Dataset, and Storage Flux Estimation

2.1 Tower-EC and Vertical Profile Measurements

To analyze the coupling between the ISL and RSL and its influence on storage flux in urban environments, we utilized tall-tower EC data along with wind and turbulence profile measurements collected in Munich during the ICOS-PAUL project. The EC system (IRGASON, Campbell Scientific Inc.), comprising an ultrasonic anemometer and an open-path infrared gas analyzer, is mounted at 85 m on a telecommunication tower (Fig. 1a). Three-dimensional wind velocities, sonic temperature, water vapor, and CO_2 concentrations are measured with a 20-Hz sampling frequency and collected by a CR6 datalogger (Campbell Scientific Inc.). Five months (Feb 1 to Jun 30, 2023) of raw data was processed by TK3 was employed to process the raw time-series data following a standardized workflow, obtaining 30-min time-averaged statistics and quality-controlled turbulent fluxes (Lan et al. 2024). A scanning Doppler Wind Lidar (Halo Photonics Streamline XR) is deployed on the rooftop of a building (8 m a.g.l), approximately 200 m southwest of the tower. The instrument was configured to obtain vertical profiles of the three-dimensional wind components through a 24-point Velocity Azimuth Display (VAD) pattern at (70°) elevation. With the technically determined range-gate length of 18 m, the vertical resolution was 16.9 m at this elevation. The maximal range of the instrument, while technically limited to 3000 m, was limited by atmospheric conditions, such as aerosol load. Due to the cone shaped geometry of the scan pattern, the horizontal area swept by the laser had radii of 34.2 m (171.0 m) at 100 m (500 m) above the instrument's aperture, respectively. One full scan was obtained roughly every 160 s, resulting in 550 profiles daily. A signal-to-noise filter of – 21 dB was applied to all data before fitting. Various data integrity tests were applied to filter data, which had too few valid samples for fitting, as well as fits resulting in high uncertainty, low velocities relative to turbulence, or large outliers. 30-min time-averaged profiles of wind speed, wind direction, and turbulent intensity (e.g., standard deviations of three-dimensional wind velocities: σ_u, σ_v, and σ_w) were then calculated. While the lowest three levels of measurements are discarded due to insufficient backscatter timescales, the scanning lidar well captures the overall wind profile (Fig. 12a). Additionally, the profiles of friction velocity (Fig. 12b) and turbulent kinetic energy (Fig. 12c–e) align with the general characteristics of those in the urban boundary layer, as evidenced by the observed maximum turbulent intensity in the RSL (Kastner-Klein and Rotach 2004; Barlow 2014). It is worth noting that the EC system is deployed in the ISL, as supported by the wind and turbulence profile measurements.

To investigate the diagnostic relationship between turbulent flux transport and storage flux, in addition to the abovementioned urban tall-tower EC measurements, one month (Jun 1 to Jun 30, 2023) of tower-EC measurements in a forest site (DE-Tha) are analyzed. The EC system, consisting of an ultrasonic anemometer (GILL-SOLENT-R3, GILL INSTRUMENTS) and a closed-path infrared gas analyzer (LI-7000, LICOR Inc.), is mounted at 42 m (Fig. 1b). Three-

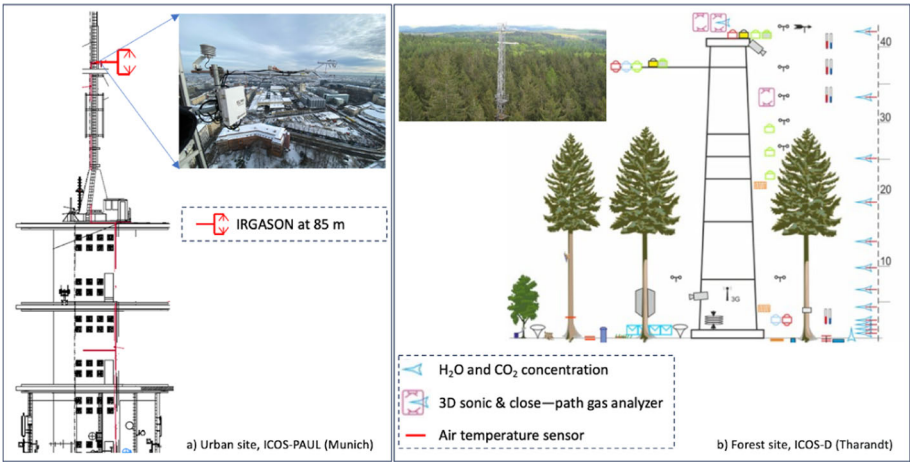

Fig. 1 Schematic illustration of **a** the location of the EC system in the urban site of the ICOS Cities project in Munich; **b** the arrangement of the EC system and profile measurements of H_2O and (CO_2) along the tower in the ICOS ecosystem forest site DE-Tha

dimensional wind velocities, sonic temperature, water vapor, and (CO_2) concentrations are measured at a 20-Hz sampling frequency and processed by the ICOS protocol (Sabbatini et al. 2018) to obtain 30-min time-averaged statistics and quality-controlled turbulent fluxes. Besides, profile measurements of air temperature, water vapor, and (CO_2) concentration are conducted at the forest site. The canopy height of the forest site is 32 m. Other site characteristics and instrument details of DE-Tha are documented on the ICOS website (https://www.icos-infrastruktur.de/en/icos-d/components/ecosystem/study-sites/tharandt-c1) and are not discussed here.

2.2 Storage Flux

The (CO_2) storage flux (F_{stor}) is determined from concentration measurements along the tower (Aubinet et al. 2005):

$$F_{stor} = \frac{1}{t}\sum_{i=0}^{n} \Delta\overline{C_\rho} z_i, \tag{1}$$

where t is the flux averaging period (i.e., 30 min) and z is the height of concentration profile measurements. $\Delta\overline{C_\rho}$ represents the integrate changes in mean (CO_2) partial density over time (i.e., 30-min in current study). Note that due to the lack of (CO_2) concentration profile measurements in the urban site, (CO_2) concentrations measured by the tower-EC system are used to estimate F_{stor} with the assumption that $\Delta\overline{C_\rho}/\Delta t$ remains constant throughout the air volume beneath the measurement height. As shown in Fig. 2a, positive F_{stor} mainly occurs during nighttime, concurrent with stable conditions. In contrast, negative F_{stor} is observed during daytime and unstable conditions, consistent with prior studies in urban and tall vegetation ecosystems (Crawford and Christen 2014; Nicolini et al. 2018). In addition, we analyzed the relationship with the results of test on integral turbulent characteristic (ITC) that is routinely conducted as part of the quality assurance and quality control of long-term EC measurements (Mauder et al. 2013). It is based on the flux-variance similarity theory

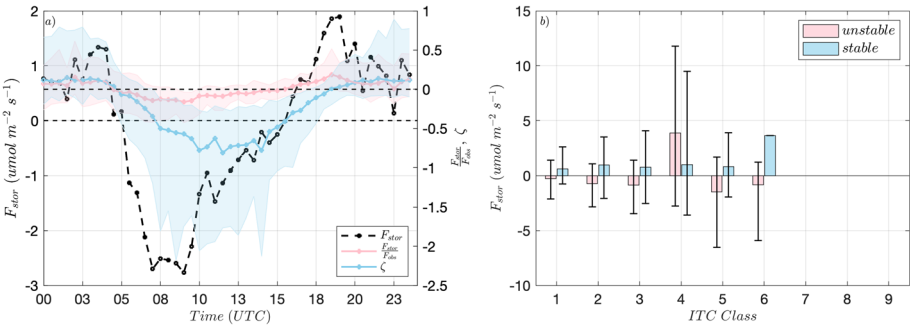

Fig. 2 **a** The median diurnal variation of (CO_2) storage flux (black dash curve), the ratio of storage flux to tower-EC measured flux (red solid curve), and the non-dimensional stability parameter (ζ, blue solid curve). The shaded areas represent the corresponding interquartile ranges. **b** The relationship between (CO_2) storage flux and the result of integral turbulence characteristic test according to the 1–9 class scheme of Foken and Wichura (1996). The error bars indicate the corresponding interquartile ranges

(Panofsky et al. 1977) and tests for well-developed turbulence (Foken and Wichura 1996). We found that a large F_{stor} is associated with large values of the ITC test result (Fig. 2b), indicating poorer data quality. This means that (CO_2) primarily emitted by near-surface sources cannot be fully transported from the RSL into the ISL when turbulence is suppressed. While a portion of large F_{stor} can be filtered out due to the ITC test, considerable F_{stor} is still observed for those fluxes which passed the data quality control processes. Therefore, given the interest in the influence of vertical coupling and turbulent transport on F_{stor}, 967 (450) segments of 30-min nighttime data measured at the urban (forest) site with a '0' quality flag based on the 0-1-2 scheme (Mauder et al. 2013) are included in the following analysis.

3 Results and Discussion

3.1 Coupling State Between ISL and RSL and the Corresponding Influence on Storage Flux

Turbulent intensity measurements from the wind lidar and the tower-EC system are employed to examine the HOST hypothesis and further investigate the coupling state between the ISL and RSL. To determine the threshold separating weak-wind and strong-wind regimes in the HOST relationship, a piece-wise linear function is employed to fit the relation between friction velocity (u_*) and bulk wind shear ($\overline{U}/z$) (Freundorfer et al. 2019):

$$u_*\left(\frac{\overline{U}}{z}\right) = \begin{cases} a_1\left(\frac{\overline{U}}{z}\right) + b_1, & \text{when } \left(\frac{\overline{U}}{z}\right) < \left(\frac{\overline{U}}{z}\right)_{thrd} \\ a_2\left(\frac{\overline{U}}{z}\right) + b_2, & \text{when } \left(\frac{\overline{U}}{z}\right) > \left(\frac{\overline{U}}{z}\right)_{thrd} \end{cases}, \tag{2}$$

Where the subscript 'thrd' denotes the bulk wind shear separating weak-wind and strong-wind regimes in the HOST relationship. Given that $b_2 = (a_1 - a_2)\left(\frac{\overline{U}}{z}\right) + b_1$, the bulk wind shear threshold can be determined as a fitting parameter along with a_1, a_2, and b_1.

Due to its adherence to the constant-flux assumption, the friction velocity (u_*) is relatively independent of height within the ISL (Fig. 12b). Therefore, only lidar measurements at 52 m

(in the RSL) and 66 m (in the ISL) are presented, together with the tower-EC measurements (Fig. 3). As expected, it is observed that the relation between u_* and bulk wind shear ($\overline{U}/z$) follows the hockey stick-like pattern (Sun et al. 2012, 2020), manifested by a slope close to zero for weak wind regimes, whereas there is a stronger increase of u_* with $\overline{U}/z$ under strong wind conditions. This salient feature suggests that the energetic turbulent eddies scaled with the observation height are primarily generated by the bulk wind shear when wind speed exceeds a certain threshold. The wind speed threshold at each height is determined by the local maximum slope in the relationship between u_* and $\overline{U}/z$ using bin-averaged quantities. Although the wind speed threshold for separating weak and strong wind regimes is height-dependent, the dataset is categorized into two corresponding subsets based on the threshold determined from the tower-EC measurements ($\overline{U}/z = 0.58\ \mathrm{s}^{-1}$) for our purpose of investigating the influence of vertical coupling on storage flux. The spectral analysis for vertical wind velocity further confirms that turbulent eddies mainly generated by the bulk shear in strong wind conditions are scaled with their measurement height, evidenced by the less-than-one frequency corresponding to the energy peak in w spectra (Fig. 4a). It indicates that these eddies can interact with the ground surface directly. In contrast, the normalized frequency is larger than one under weak wind conditions, indicative of the turbulent eddies detached of the surface, leading to the so-called "z-less" scaling, and consequently flux gradients are expected (Nieuwstadt 1984; Babić et al. 2016; Lan et al. 2018).

To further investigate the coupling between the ISL and RSL, the relationship of cross-layer σ_w is further examined. Similar to results reported in prior forest studies (Thomas et al. 2013; Jocher et al. 2018, 2020), Figure 4b shows that in strong wind conditions and $\sigma_{w,RSL} < 1.25\ \mathrm{ms}^{-1}$, σ_w in the ISL is linearly dependent on the counterpart in RSL, suggesting the coupling between the ISL and RSL, consistent with the observed features in forests (Freundorfer et al. 2019; Jocher et al. 2020). When $\sigma_{w,RSL} > 1.25\ \mathrm{ms}^{-1}$, however, the relation between $\sigma_{w,ISL}$ and $\sigma_{w,RSL}$ has a slope close to zero, a hallmark for decoupling. Note that the threshold of $\sigma_{w,RSL}$ is also determined from the bin-averaged curve, with each bin containing no fewer than 50 data points. Under weak wind conditions, a monotonic increase in $\sigma_{w,ISL}$ as a function of $\sigma_{w,RSL}$ is observed, despite a relatively smaller slope when $\sigma_{w,RSL} > 0.9\ \mathrm{ms}^{-1}$. This finding is distinct from those reported in forest studies suggesting that weak wind regimes go along with the decoupling between ISL and RSL. However, it can be explained by the profiles of normalized shear production and transport terms in the TKE budget equation (Fig. 5).

Given that air communicates across all TKE sinks and sources in the vertical, small TKE gradient is expected, indicative of the coupling between ISL and RSL (e.g., $\sigma_{w,RSL} < 1.25\ \mathrm{ms}^{-1}$). This coupling between ISL and RSL is supported by the linear dependence of $\sigma_{w,ISL}$ for $\sigma_{w,RSL}$. As a consequence, the storage fluxes are smaller than the counterparts when $\sigma_{w,RSL} > 1.25\ \mathrm{ms}^{-1}$, even in weak wind regimes (Fig. 6). Besides, the magnitude of storage flux is nearly independent of wind speed under weak wind conditions, while a prominent drop in storage flux is observed in strong wind regimes. When the vertical TKE gradient enlarges (e.g., $\sigma_{w,RSL} > 1.25\ \mathrm{ms}^{-1}$), suppressed shear-produced turbulence is observed (relatively smaller value of the TKE shear production term, Fig. 5a), leading to the decoupling between ISL and RSL. Therefore, relatively large storage fluxes are observed in weak wind regimes, together with dependence on the wind speed. Conversely, TKE within the RSL is transported upward to the ISL when wind speed exceeds the threshold (positive value of the TKE transport term, Fig. 5b), conducive to the coupling between ISL and RSL as predicted by the HOST relationship. As a result, the magnitude of storage flux is comparable to its counterpart when $\sigma_{w,RSL} < 1.25\ \mathrm{ms}^{-1}$. Such dependence of storage flux on the TKE gradient will be further supported in the following theoretical argument.

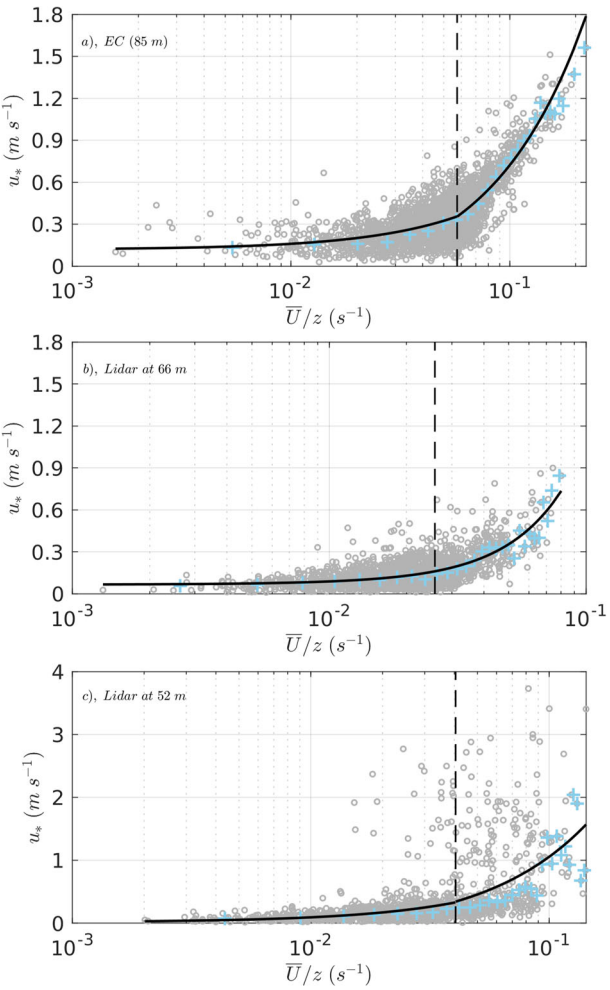

Fig. 3 The friction velocity as a function of bulk wind shear at the tower-EC measurement height (**a**), in the inertial sub-layer (**b**), and roughness sub-layer (**c**) in the urban site. Grey circles represent all nighttime measurements, while blue markers represent the binned median values for nighttime measurements. The solid black curve denotes the bin-average fitting curve calculated using bins with no fewer than 50 data points each. The vertical dashed line indicates the wind speed threshold at which the linear relationship between turbulent intensity and bulk wind shear becomes more prominent

3.2 Theoretical Argument on the Relation Between Turbulent Flux Transport and Storage Flux

The influence of the storage flux can be investigated based on the budget equation of the CO_2 flux ($\overline{w'c'}$). For stationary and planar-homogeneous atmospheric surface layer flows with negligible molecular dissipation, the budget equation of $\overline{w'c'}$ is expressed as (Stull 2012):

$$\frac{\partial \overline{w'c'}}{\partial t} = 0 = -\overline{w'^2}\frac{\partial \overline{c}}{\partial z} + \overline{c'\theta'}\frac{g}{\overline{\theta}} - \frac{\partial \overline{w'w'c'}}{\partial z} - \frac{1}{\rho}\overline{p'\frac{\partial c'}{\partial z}}. \tag{3}$$

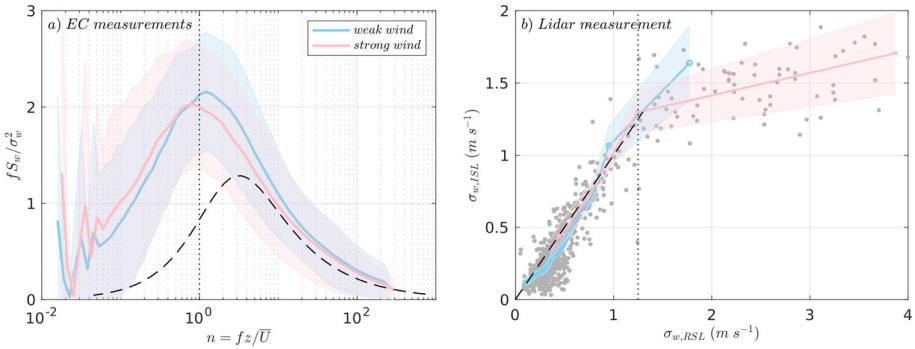

Fig. 4 **a** The normalized variance spectra for the vertical wind velocity under weak and strong wind conditions. The vertical velocity spectra are computed from EC measurements. The shaded areas and the dash curve represent the corresponding interquartile ranges and the model spectra under near-neutral conditions based on the Kansas experiment, respectively (Kaimal et al. 1972). **b** The vertical turbulent intensity in the inertial sub-layer ($\sigma_{w,ISL}$) as a function of its counterpart in the roughness sub-layer ($\sigma_{w,RSL}$). The standard deviation of vertical velocity in the ISL and RSL are determined from Lidar measurements. The dashed line indicates the linear dependence of $\sigma_{w,ISL}$ on $\sigma_{w,RSL}$. The vertical dot line denotes the threshold in $\sigma_{w,RSL}$ (1.25 ms^{-1}) at which turbulence in the inertial sub-layer becomes independent from that in the roughness sub-layer. The gray dots represent nighttime measurements in both weak-wind and strong-wind regimes

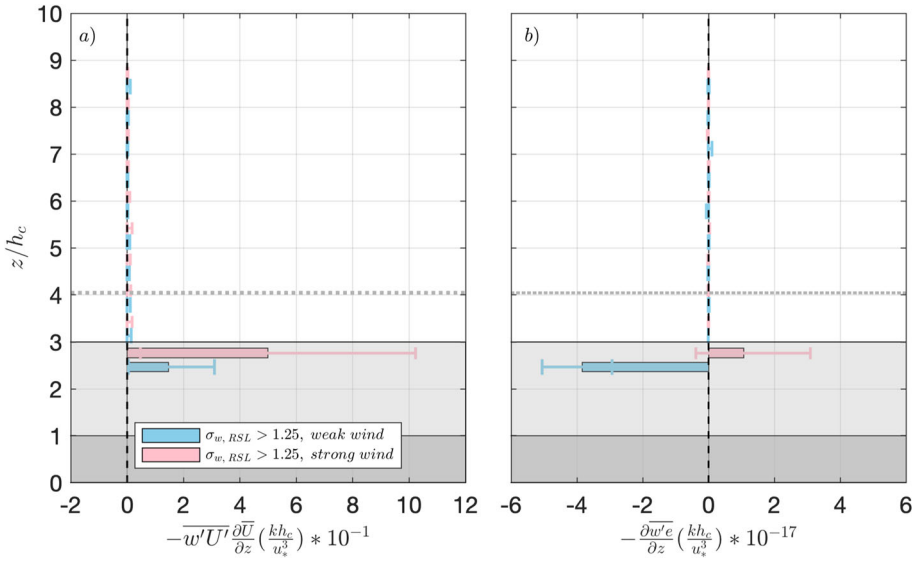

Fig. 5 Vertical profiles of the median of normalized shear-production (**a**) and vertical transport term (**b**) in the turbulent kinetic energy (TKE) budget equation. k, h_c, and u_* are the von Kármán constant, canopy height, and friction velocity, respectively. The error bars indicate the corresponding interquartile ranges. The profiles corresponding to strong wind cases are slightly shifted upward for readability

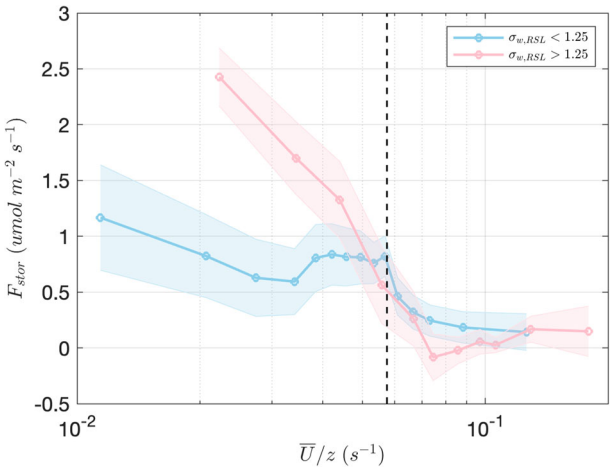

Fig. 6 The friction velocity as a function of bulk wind shear at the tower-EC measurement height in the urban site. The shaded areas represent the corresponding interquartile ranges

The terms on the right-hand side (RHS) of Eq. (3) include i) the production term associated with the mean concentration profile of CO_2 ($-\overline{w'^2}\frac{\partial \overline{c}}{\partial z}$); (ii) the buoyancy term associated with thermal stratification ($\overline{c'\theta'}\frac{g}{\overline{\theta}}$); (iii) the third-order turbulent flux transport term ($-\frac{\partial \overline{w'w'c'}}{\partial z}$); iv) the pressure decorrelation term ($-\frac{1}{\rho}\overline{p'\frac{\partial c'}{\partial z}}$). The pressure decorrelation term can be parameterized by the Rotta model which retains the linear component (Rotta 1951):

$$-\frac{1}{\rho}\overline{p'\frac{\partial c'}{\partial z}} = -\frac{\overline{w'c'}}{\tau_c}, \tag{4}$$

where τ_c represents the relaxation time scale delineating how fast a turbulent eddy loses its coherence (Li 2019). Then, $\overline{w'c'}$ can be solved as:

$$\overline{w'c'} = \tau_c\left(-\overline{w'^2}\frac{\partial \overline{c}}{\partial z} - \frac{\partial \overline{w'w'c'}}{\partial z} + \overline{c'\theta'}\frac{g}{\overline{\theta}}\right). \tag{5}$$

Employing the cumulant expansion method (CEM, e.g., (Raupach and Thom 1981; Nagano and Tagawa 1995; Katul et al. 1997)) for parameterization of the third-order flux transport term ($\overline{w'w'c'} = f u_* \overline{w'c'}$, where f quantifies the influence of large coherent eddies on vertical flux transport) and involving the scalar transport similarity between CO_2 and kinematic heat ($R_{c\theta} = \frac{\overline{c'\theta'}}{\sigma_c \sigma_\theta}$), Eq. (5) can be rewritten as:

$$f\frac{\partial \overline{w'c'}}{\partial z} + \overline{w'c'}\left(\frac{\partial f}{\partial z} + \frac{f}{u_*}\frac{\partial u_*}{\partial z} + \frac{1}{\tau_c u_*}\right) = -\frac{\overline{w'^2}}{u_*}\frac{\partial \overline{c}}{\partial z} + \frac{g}{\overline{\theta}}\frac{R_{c\theta}\sigma_c\sigma_\theta}{u_*}. \tag{6}$$

Multiplying $\frac{kz}{u_*^2 c_* \theta_*}$ (k and z are von Kármán constant and measurement height, respectively; $c_* = -\frac{(\overline{w'c'})_{surf}}{u_*}$ and $\theta_* = -\frac{(\overline{w'\theta'})_{surf}}{u_*}$ are surface scaling parameter for CO_2 and temperature, respectively) for both sides of Eq. (6) yields (refer to Appendix 3 for detail derivation):

$$f\frac{\partial h_{c,stor}}{\partial z}+(1+h_{c,stor})\left(\frac{\partial f}{\partial z}+\frac{f}{u_*}\frac{\partial u_*}{\partial z}+\frac{1}{\tau_c u_*}\right)=\frac{1}{kz}\left(\phi_{ww}^2\phi_c-\zeta\Re\phi_{\theta\theta}^2\frac{1}{1+h_{\theta,stor}}\right), \tag{7}$$

where $\phi_{ww}=\frac{\sigma_w}{u_*}$ and $\phi_{\theta\theta}=\frac{\sigma_\theta}{\theta_*}$ $\phi_{\theta\theta}=\frac{\sigma_\theta}{\theta_*}$ are the flux-variance relationships for vertical velocity and temperature, respectively, as functions of non-dimensional stability parameter $\zeta=\frac{z}{L}$ ($L=-\frac{u_*^3}{kg\overline{w'\theta'}}$) is the Obukhov length, where g is gravitational acceleration); $\phi_c=\frac{kz}{c_*}\frac{\partial\overline{c}}{\partial z}$ is the non-dimensional CO_2 concentration gradient as a function of ζ expressed in terms of Monin–Obukhov similarity theory (MOST, (Monin and Obukhov 1954)); $\Re=\frac{\theta_*}{c_*}\frac{\overline{\theta'c'}}{\sigma_\theta^2}$; $h_{c,stor}=\frac{(\overline{w'c'})_{stor}}{(\overline{w'c'})_{surf}}$ and $h_{\theta,stor}=\frac{(\overline{w'\theta'})_{stor}}{(\overline{w'\theta'})_{surf}}$, the subscripts 'stor' and 'surf' denote the storage flux and the flux at ground surface. It implies that both $h_{c,stor}$ and $h_{\theta,stor}$ are identically zero if the MOST is valid (i.e., assumptions of flow stationarity, constant-flux, and transport similarity are fulfilled), which underpins the EC measurement.

As predicted by the K-theory ($\overline{w'w'c'}=K\frac{\partial\overline{w'c'}}{\partial z}$, (Stull 2012)), the third-order flux transport term equals zero when the vertical flux gradient is negligible. Consequently, negligible storage flux is expected ($h_{c,stor}=0$), equivalent to $f=0$ as predicted by the CEM. The normalized relaxation time scale can be solved from Eq. (7), as the only function of ζ:

$$T_{c1}=\frac{\tau_c u_*}{kz}=\left(\phi_{ww}^2\phi_c-\zeta\Re\phi_{\theta\theta}^2\frac{1}{1+h_{\theta,stor}}\right)^{-1}. \tag{8}$$

However, finite vertical flux transport has been observed even though the vertical flux gradient is negligible (Katul et al. 1997; Cava et al. 2006; Ghannam et al. 2017). Such finite vertical flux transport is primarily attributed to large coherent eddies that contribute asymmetrically to flux by sweeps and ejections. Given the scenario of negligible storage flux and f deviating from zero, substituting Eq. (8) into Eq. (7) and employing the flux-variance relationship for vertical velocity ($\phi_{ww}(\zeta)=\frac{\sigma_w}{u_*}$) yield:

$$kz\frac{\partial f}{\partial z}=T_{c1}^{-1}-T_{c2}^{-1}-kzf\frac{\partial\ln(\sigma_w)}{\partial z}, \tag{9}$$

where T_{c2} is also only a function of stability, representing the normalized relaxation time scale. It is worth noting that $T_{c1}=T_{c2}$ is not mandatory as the finite turbulent flux transport term may interact with the relaxation time scale of the Rotta model (Rotta 1951). Based on the identity of $z\frac{\partial f}{\partial z}=\zeta\frac{\partial f}{\partial\zeta}$, the sufficient condition for negligible storage flux can be derived as:

$$k\zeta\frac{\partial f}{\partial\zeta}=T_{c1}^{-1}-T_{c2}^{-1}-kzf\frac{\partial\ln(\sigma_w)}{\partial z}=0. \tag{10}$$

Combining Eqs. (7), (8), (9), (10) reveals that the storage flux is mainly modulated by ζ and the vertical gradient of TKE ($\frac{\partial\ln(\sigma_w)}{\partial z}$), further confirming the qualitative findings in the previous section (e.g., Fig. 2a and Fig. 6).

3.3 Diagnostic Function for the Negligible Storage Flux

To derive the diagnostic function for negligible storage flux, the performance of CEM is first evaluated, which is the prerequisite for parameterizing the third-order flux transport term in Eq. (4). As f is a measure of the asymmetry between sweeps and ejections associated with

large coherent eddies, it is generally parameterized by the incomplete cumulant expansion method (ICEM, e.g., (Cava et al. 2006; Banerjee et al. 2017; Katul et al. 2018):

$$f = 2\sqrt{2\pi}\frac{\Delta S_0 \phi_{ww}}{\gamma}, \tag{11}$$

where $\Delta S_0 = S_{sweep} - S_{ejection}$ represents the imbalance of flux contribution caused by sweeps and ejections, ranging from – 1 to 1; $R_{wc} = \frac{\overline{w'c'}}{\sigma_w \sigma_c}$ is the transport efficiency of (CO_2); $\gamma = \frac{M_{21}}{M_{12}-1}$ indicates the ratio of the dimensionless turbulent transport of (CO_2) flux and the dimensionless turbulent transport of the (CO_2) variance, where $M_{12} = \frac{\overline{w'c'c'}}{\sigma_w \sigma_c^2}$ and $M_{21} = \frac{\overline{w'w'c'}}{\sigma_w^2 \sigma_c}$. Figure 7 a and c show the comparison of measured and modeled ΔS_0 for the urban and forest site, respectively. The measured ΔS_0 is determined by an improved quadrant analysis as discussed by Wang et al. (2022), while modeled $\Delta S_0 = \frac{M_{21}-M_{12}}{2\sqrt{2}R_{wc}}$ (where $R_{wc} = \frac{\overline{w'c'}}{\sigma_w \sigma_c}$), as predicted by the ICEM (Wang et al. 2014). The ΔS_0 between measurements and ICEM predictions are in good agreement, especially when imposing controls in terms of storage flux. This finding lends support to employing CEM to parameterize the third-order flux transport term, further confirmed by the good agreement of f between measurements and ICEM approximation (Fig. 7b and d). Compared to the urban site, the data points corresponding to the forest site exhibit a relatively larger scatter, possibly attributed to the EC measurement conducted in the RSL over the forest. Nevertheless, the comparisons support that the ICEM reflects the influence of large coherent eddies on vertical flux transport over a variety of landscapes, consistent with previous studies (Wang et al. 2014; Katul et al. 2018).

The variations of f, T_{c1}, and T_{c2} with ζ as well as the linkage to storage flux are further explored. Figure 8 shows the relations of ϕ_{ww}, ΔS_0, M_{21}, and M_{12} as a function of ζ. It is evident that the scatter of data points is largely reduced when storage flux is 'negligible' (e.g., $|\frac{F_{stor}}{F_{obs}}| < 5\%$ for the urban site). Additionally, all variables for parameterizing f become explicit functions of ζ as provided in Table 1. To determine the explicit function of T_{c1} to ζ, the assumption that negligible storage flux for kinematic heat coexists with negligible storage flux for (CO_2) is required. On the one hand, determining the storage flux for kinematic heat in the urban site is challenging due to the complex thermal capacity of the urban fabric (Grimmond and Ward 2021); on the other hand, this assumption has intrinsic link to the transport similarity hypothesized by the MOST. Moreover, due to the intermittent respiration bursts of (CO_2), approximating the non-dimensional (CO_2) gradient by the stability function is difficult (Fig. 13a). Hence, the Businger-Dyer relationship (Businger et al. 1971; Dyer and Hicks 1970) for parameterizing the non-dimensional temperature gradient (ϕ_h) is adopted to approximate ϕ_c (Fig. 13b). Although substantial scatter in the relation between $\Re$ and ζ was reported in (Katul et al. 2016), our data show that the scatter is significantly reduced when considering $\zeta\Re$ or $\zeta\Re\phi_\theta^2$ as a function of ζ (Fig. 9). This finding implies that, compared to $\Re$ and ϕ_θ^2, $\zeta\Re$ has a more important contribution to the variation of T_{c1}. The explicit function of T_{c1} with respect to ζ is also provided in Table 1.

By employing the identity of $z\frac{\partial \ln(\sigma_w)}{\partial z} = \zeta\frac{\partial \ln(\sigma_w)}{\partial \zeta}$, the influence of σ_w gradient on storage flux is reflected by the relation between $ln(\sigma_w)$ and ζ using the tower-EC measurements (Fig. 10). From one perspective, $ln(\sigma_w)$ increases with enhancing wind speed as predicted by the HOST framework; its increasing rate, from another perspective, reduces under strong wind regimes and weakened stratification, evidenced by the near-zero local slope of the bin-averaged fitting curve. This finding further confirms the previously observed phenomenon that finite storage flux occurs when the gradient of TKE between ISL and RSL is small.

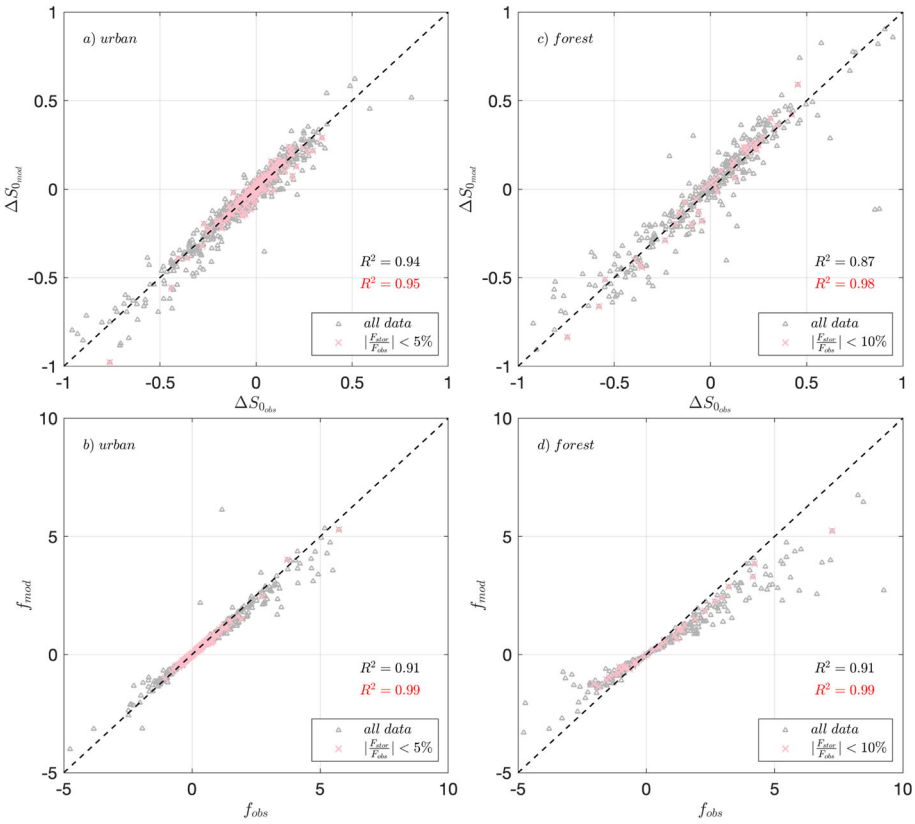

Fig. 7 The comparison of measured and modeled ΔS_0 and f for (CO_2) in the urban (**a** and **b**) and forest sites (**c** and **d**). The grey markers represent cases when no control on data regarding the storage flux, while the red markers represent cases with the ratio of storage flux to tower-EC flux within 5% for the urban site (10% for the forest site)

Table 1 The least-square fitting functions for variation of ϕ_{ww}, ΔS_0, M_{21}, M_{12}, γ, $\zeta\Re$, $\zeta\Re\phi_\theta^2$ with ζ

Fitting functions	
With control	Without control
$\phi_{ww} = 1.27(1+0.24\zeta)^{1/3}$	$\phi_{ww} = 1.26(1+0.33\zeta)^{1/3}$
$\Delta S_0 = 0.21(e^{-0.39\zeta} - 1)$	$\Delta S_0 = 0.82(e^{-0.03\zeta} - 1)$
$M_{21} = -0.02\zeta^{-0.32}$	$M_{21} = 0.02\zeta^{-0.04}$
$M_{12} = -0.10\zeta^{0.34}$	$M_{12} = -0.10\zeta^{0.38}$
$\gamma = 0.20\zeta^{1/3} - 1$	$\gamma = -0.20\zeta^{-0.42} - 1$
$\zeta\Re = \frac{1.59}{1+e^{-0.59\zeta}}$	$\zeta\Re = \frac{0.44}{1+e^{-0.01\zeta}}$
$\zeta\Re\phi_\theta^2 = \frac{1.59}{1+e^{-0.59\zeta}}(0.94\zeta^{0.56})^2$	$\zeta\Re\phi_\theta^2 = \frac{0.44}{1+e^{-0.01\zeta}}(1.95\zeta^{0.89})^2$

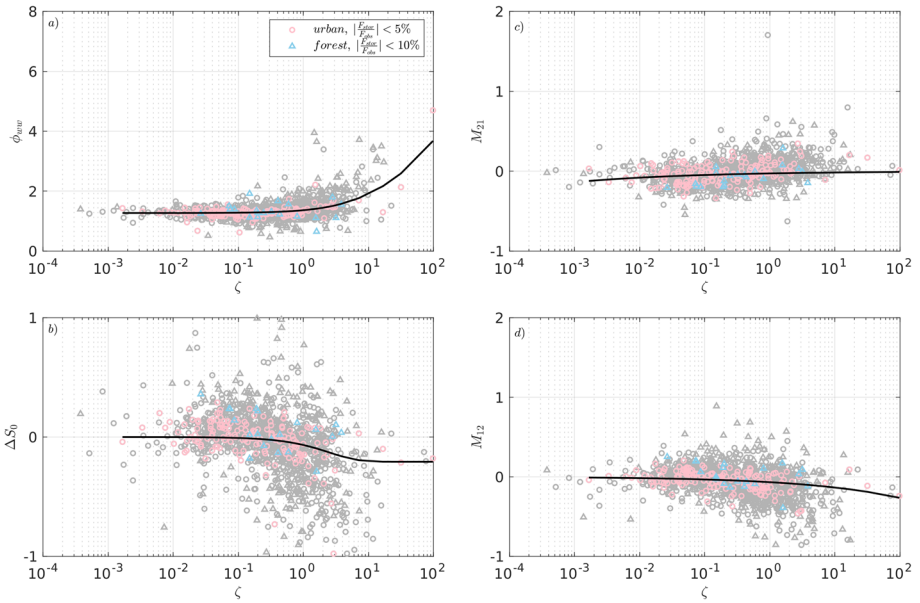

Fig. 8 The variation of ϕ_{ww} (**a**), ΔS_0 (**b**), M_{21} (**c**), and M_{12} (**d**) with ζ in the urban (circles) and forest sites (triangles). The grey markers represent cases with no control on data regarding the storage flux, while the red markers represent cases with the ratio of storage flux to tower-EC flux within 5% for the urban site (10% for the forest site). Black curves represent the least-square fitting functions provided in Table 1

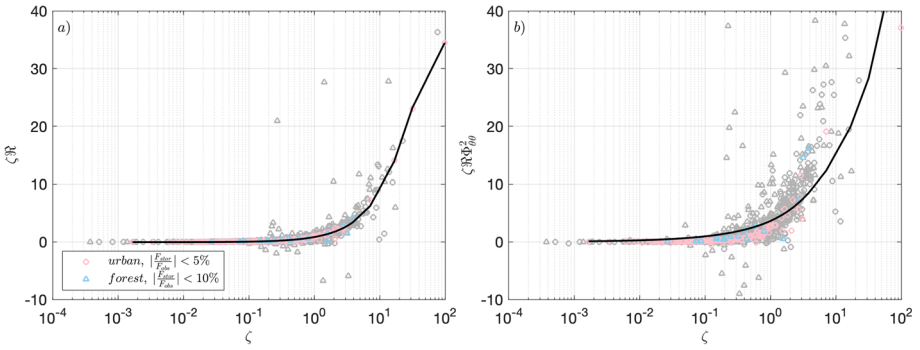

Fig. 9 The variation of $\zeta\Re$ (**a**) and $\zeta\Re\phi_\theta^2$ (**b**) with ζ in the urban (circles) and forest sites (triangles). The grey markers represent cases with no control on data regarding the storage flux, while the red markers represent cases with the ratio of storage flux to tower-EC flux within 5% for the urban site (10% for the forest site). Black curves represent the least-square fitting functions provided in Table 1

Accordingly, the sufficient condition for negligible storage flux (Eq. 9) can be simplified as:

$$k\zeta\frac{\partial f}{\partial z} = T_{c1}^{-1} - T_{c2}^{-1} = 0 \tag{12}$$

Based on the fitting functions provided in Table 1, Fig. 11 presents the variation of f, $k\zeta\frac{\partial f}{\partial z}$, T_{c1}^{-1}, and T_{c2}^{-1} under stable conditions. It is evident that f increases from zero with increasing stability, indicative of the prominent influence of large coherent eddies on flux transport,

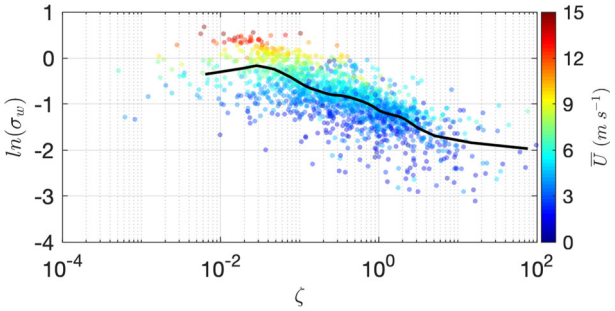

Fig. 10 The variation of vertical turbulent intensity (ln (σ_w)) with ζ at the tower-EC measurement height in the urban site. The black curve represents the bin-averaged fitting curve, with each bin containing no fewer than 50 data points

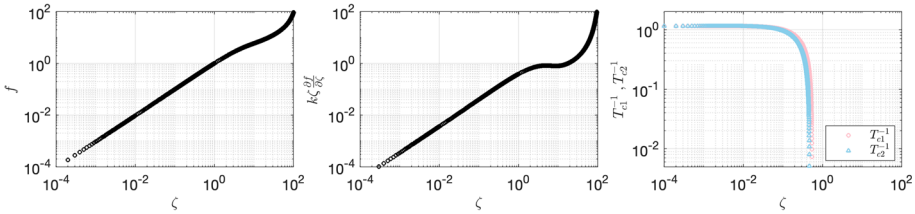

Fig. 11 $f, k\zeta\frac{\partial f}{\partial z}, T_{c1}^{-1}$, and T_{c2}^{-1} as explicit functions of ζ computed using the fitting functions provided in Table 1

consistent with previous studies (Cuxart et al. 2002; Cooper et al. 2006; Barthlott et al. 2007). The $k\zeta\frac{\partial f}{\partial z}$ deviates from near-zero value concurring with the increasing f, implying that storage flux becomes considerable in stable conditions despite T_{c1}^{-1} and T_{c2}^{-1} approaching zero. For another extreme, T_{c1}^{-1} and T_{c2}^{-1} become identical in near-neutral conditions and $k\zeta\frac{\partial f}{\partial z}$ approaches zero, and thus negligible storage flux is expected.

4 Conclusions

Utilizing the urban tall-tower EC data alongside profile measurements from a collocated scanning wind lidar, we investigated the coupling between ISL and RSL, and its subsequent influence on nighttime storage flux. Our findings reveal that the turbulent intensity varies with wind speed as delineated by the HOST framework. In strong wind regimes, turbulent eddies primarily generated by bulk wind shear directly interact with the ground surface, whereas in weak wind conditions, turbulence eddies detach from the surface. The relationship between σ_w in ISL and RSL highlights the role of turbulent transport in regulating the vertical coupling. When the vertical gradient of TKE between ISL and RSL enlarges, shear-generated turbulence is suppressed, leading to decoupling between the ISL and RSL and consequently, large storage fluxes are observed. With increasing wind speed, turbulent eddies with scales comparable to the measurement height transport TKE upward to the ISL, reducing the TKE gradient, and thus promoting coupling between ISL and RSL. Consequently, the storage flux decreases dramatically and maintains relatively low values when the wind speed exceeds the threshold predicted by the HOST relationship. The theoretical argument supports the

notion that nighttime storage flux is primarily regulated by the atmospheric stability and vertical TKE gradient. We further derived a diagnostic function for negligible storage flux, which can be extended to forest sites. However, it is important to point out that this diagnostic relation is based on assumptions of negligible advection and scalar transport similarity, which are rarely observed in heterogeneous urban landscapes. Therefore, a temporal-spatial flux mapping approach (Metzger et al. 2013; Metzger 2018; Xu et al. 2017, 2018) is necessary for estimating fluxes that meet the basic assumptions of the EC technique and for re-evaluating the proposed diagnostic relation, which will be the compass for our future work.

Appendix 1: Profile measurements from scanning Doppler Lidar

See Fig. 12.

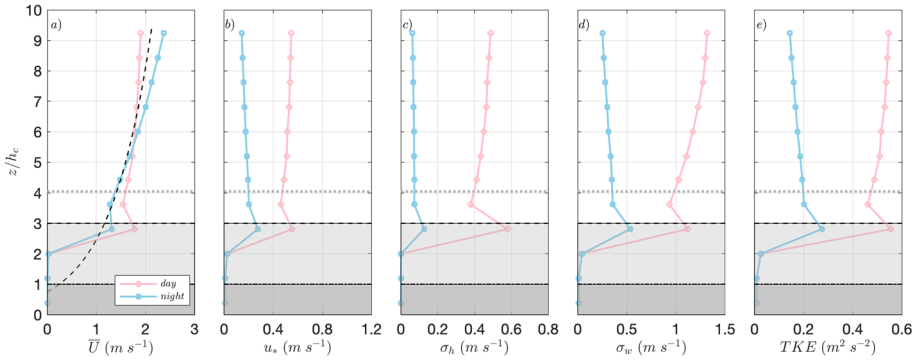

Fig. 12 Median daytime (red curve) and nighttime (blue curve) profiles of: **a** horizontal wind speed; the black dash curve represents the modeled logarithmic wind profile in neutral conditions; **b** friction velocity (u_*); **c** horizontal turbulent intensity ($\sigma_h = \sqrt{\sigma_u^2 + \sigma_v^2}$), where σ_u and σ_v are the standard deviation of horizontal velocity components); **d** vertical turbulent intensity (σ_w); **e** turbulent kinetic energy ($TKE = \frac{1}{2}(\sigma_u^2 + \sigma_v^2 + \sigma_w^2)$). Only lidar measurement data below 200 m are shown, considering our interest in the coupling between the inertial sub-layer and roughness sub-layer. The measurement height is normalized by the canopy height ($h_c = 20\ m$). The shaded areas denote the range of urban canopy layer (dark grey) and roughness sub-layer (light grey), respectively. The horizontal grey dash line indicates the measurement height of the tower-EC system

Appendix 2: Non-Dimensional Gradients of (CO_2) and Temperature Determined by Profile Measurements in the Forest Site

See Fig. 13.

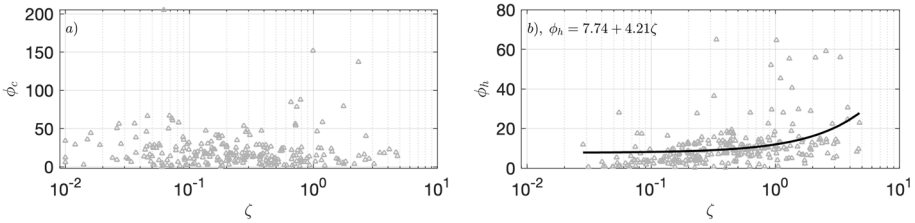

Fig. 13 The variation of ϕ_c (**a**) and ϕ_h (**b**) with ζ in the forest site. The black curve in subplot b represents the fitting function between ϕ_h and ζ following the Businger-Dyer relationship (Businger et al. 1971; Dyer and Hicks, 1970) with coefficients determined by the least-square fit

Appendix 3: Linking Storage Flux ($h_{c,stor}$) to the Flux Gradient

Multiplying $\frac{kz}{u_*^2 c_* \theta_*}$ (k and z for both sides of Eq. 6, given that $c_* u_* = -(\overline{w'c'})_{surf}$, the left-hand-side (LHS) can be rewritten as:

$$LHS*\left(\frac{kz}{u_*^2 c_* \theta_*}\right) = -f\frac{kz}{u_* \theta_*}\frac{1}{(\overline{w'c'})_{surf}}\frac{\partial \overline{w'c'}}{\partial z} - \frac{kz}{u_* \theta_*}\frac{\overline{w'c'}}{(\overline{w'c'})_{surf}}\left(\frac{\partial f}{\partial z} + \frac{f}{u_*}\frac{\partial u_*}{\partial z} + \frac{1}{\tau_c u_*}\right). \tag{A3.1}$$

Given that $(\overline{w'c'})_{surf}$ is a constant with respect to z, Eq. (A3.1) can be further rewritten as:

$$LHS*\left(\frac{kz}{u_*^2 c_* \theta_*}\right) = -f\frac{kz}{u_* \theta_*}\frac{\partial\left(\frac{\overline{w'c'}}{(\overline{w'c'})_{surf}}\right)}{\partial z} - \frac{kz}{u_* \theta_*}\frac{\overline{w'c'}}{(\overline{w'c'})_{surf}}\left(\frac{\partial f}{\partial z} + \frac{f}{u_*}\frac{\partial u_*}{\partial z} + \frac{1}{\tau_c u_*}\right). \tag{A3.2}$$

Considering that the measured flux at a given height equals the sum of surface flux and storage flux (i.e., $\overline{w'c'} = (\overline{w'c'})_{surf} + (\overline{w'c'})_{stor}$), $\frac{\overline{w'c'}}{(\overline{w'c'})_{surf}}$ can be written as:

$$\frac{\overline{w'c'}}{(\overline{w'c'})_{surf}} = \frac{(\overline{w'c'})_{surf} + (\overline{w'c'})_{stor}}{(\overline{w'c'})_{surf}} = 1 + h_{c,stor}. \tag{A3.3}$$

Substituting Eq. (A3.3) into Eq. (A3.2) yields:

$$LHS*\left(\frac{kz}{u_*^2 c_* \theta_*}\right) = -f\frac{kz}{u_* \theta_*}\frac{\partial h_{c,stor}}{\partial z} - (1 + h_{c,stor})\left(\frac{\partial f}{\partial z} + \frac{f}{u_*}\frac{\partial u_*}{\partial z} + \frac{1}{\tau_c u_*}\right). \tag{A3.4}$$

For the right-hand-side (RHS) of Eq. (6):

$$RHS*\left(\frac{kz}{u_*^2 c_* \theta_*}\right) = -\frac{\overline{w'^2}}{u_*}\frac{kz}{u_*^2 c_* \theta_*}\frac{\partial \overline{c}}{\partial z} + \frac{R_{c\theta}\sigma_c\sigma_\theta}{u_*}\frac{kz}{u_*^2 c_* \theta_*}\frac{g}{\overline{\theta}}. \tag{A3.5}$$

Rewriting Eq. (A3.5) yields:

$$RHS*\left(\frac{kz}{u_*^2 c_* \theta_*}\right) = -\frac{\overline{w'^2}}{u_*}\frac{1}{u_* \theta_*}\frac{kz}{c_*}\frac{\partial \overline{c}}{\partial z} + R_{c\theta}\frac{kz}{u_*^3}\frac{g}{\overline{\theta}}\frac{\sigma_c\sigma_\theta}{c_* \theta_*} = -\phi_{ww}^2\frac{1}{u_* \theta_*}\phi_c + R_{c\theta}\phi_{cc}\phi_{\theta\theta}\frac{kz}{u_*^3}\frac{g}{\overline{\theta}}. \tag{A3.6}$$

Introducing $\zeta = z/L$ (where $L = -\frac{u_*^3}{kg\overline{w'\theta'}}$), the second term in the RHS of Eq. (A3.6) can be rewritten as:

$$R_{c\theta}\phi_{cc}\phi_{\theta\theta}\frac{kz}{u_*^3}\frac{g}{\overline{\theta}} = -R_{c\theta}\phi_{cc}\phi_{\theta\theta}\frac{kz\frac{g}{\overline{\theta}}}{u_*^3}(-\overline{w'\theta'})\frac{1}{\overline{w'\theta'}} = -R_{c\theta}\phi_{cc}\phi_{\theta\theta}\zeta\frac{(\overline{w'\theta'})_{surf}}{\overline{w'\theta'}}\frac{1}{(\overline{w'\theta'})_{surf}}. \tag{A3.7}$$

Analogy to Eq. (A3.3) and substituting Eq. (A3.7) into Eq. (A3.6) yield:

$$RHS * \left(\frac{kz}{u_*^2 c_* \theta_*}\right) = -\phi_{ww}^2\phi_c\frac{1}{u_*\theta_*} + R_{c\theta}\phi_{cc}\phi_{\theta\theta}\zeta\frac{1}{1+h_{\theta,stor}}\frac{1}{u_*\theta_*}. \tag{A3.8}$$

Combining Eqs. (A3.4) and (A3.8) yields:

$$f\frac{\partial h_{c,stor}}{\partial z} + (1+h_{c,stor})\left(\frac{\partial f}{\partial z} + \frac{f}{u_*}\frac{\partial u_*}{\partial z} + \frac{1}{\tau_c u_*}\right) = \frac{1}{kz}\left(\phi_{ww}^2\phi_c - R_{c\theta}\phi_{cc}\phi_{\theta\theta}\zeta\frac{1}{1+h_{\theta,stor}}\right). \tag{A3.9}$$

Involving $\Re = \frac{\theta_*}{c_*}\frac{\overline{\theta' c'}}{\sigma_\theta^2}$ and $R_{c\theta} = \frac{\overline{c'\theta'}}{\sigma_c\sigma_\theta}$, Eq. (A3.9) can be rewritten as:

$$f\frac{\partial h_{c,stor}}{\partial z} + (1+h_{c,stor})\left(\frac{\partial f}{\partial z} + \frac{f}{u_*}\frac{\partial u_*}{\partial z} + \frac{1}{\tau_c u_*}\right) = \frac{1}{kz}\left(\phi_{ww}^2\phi_c - \zeta\Re\phi_{\theta\theta}^2\frac{1}{1+h_{\theta,stor}}\right). \tag{A3.10}$$

Identity to Eq. (7) in the manuscript.

Acknowledgements The authors have received funding from ICOS Cities, a.k.a. the Pilot Applications in Urban Landscapes-Towards integrated city observatories for greenhouse gases (PAUL) project, from the European Union's Horizon 2020 research and innovation program under grant agreement no. 101037319.

Funding Open Access funding enabled and organized by Projekt DEAL.

References

Acevedo OC, Moraes OL, Degrazia GA, Fitzjarrald DR, Manzi AO, Campos JG (2009) Is friction velocity the most appropriate scale for correcting nocturnal carbon dioxide fluxes? Agric For Meteorol 149(1):1–10

Aubinet M, Berbigier P, Bernhofer C, Cescatti A, Feigenwinter C, Granier A, Grünwald T, Havrankova K, Heinesch B, Longdoz B et al (2005) Comparing CO_2 storage and advection conditions at night at different carboeuroflux sites. Boundary-Layer Meteorol 116:63–93

Babić K, Rotach MW, Klaić ZB (2016) Evaluation of local similarity theory in the wintertime nocturnal boundary layer over heterogeneous surface. Agric For Meteorol 228:164–179

Banerjee T, De Roo F, Mauder M (2017) Connecting the failure of k theory inside and above vegetation canopies and ejection-sweep cycles by a large-eddy simulation. J Appl Meteorol Climatol 56(12):3119–3131

Barlow JF (2014) Progress in observing and modelling the urban boundary layer. Urban Clim 10:216–240

Barthlott C, Drobinski P, Fesquet C, Dubos T, Pietras C (2007) Long-term study of coherent structures in the atmospheric surface layer. Boundary-Layer Meteorol 125:1–24

Businger JA, Wyngaard JC, Izumi Y, Bradley EF (1971) Flux-profile relationships in the atmospheric surface layer. J Atmos Sci 28(2):181–189

Cava D, Katul G, Scrimieri A, Poggi D, Cescatti A, Giostra U (2006) Buoyancy and the sensible heat flux budget within dense canopies. Boundary-Layer Meteorol 118:217–240
Cooper D, Leclerc M, Archuleta J, Coulter R, Eichinger W, Kao C, Nappo C (2006) Mass exchange in the stable boundary layer by coherent structures. Agric For Meteorol 136(3–4):114–131
Crawford B, Christen A (2014) Spatial variability of carbon dioxide in the urban canopy layer and implications for flux measurements. Atmos Environ 98:308–322
Cuxart J, Morales G, Terradellas E, Yagüe C (2002) Study of coherent structures and estimation of the pressure transport terms for the nocturnal stable boundary layer. Boundary-Layer Meteorol 105:305–328
Davis KJ, Deng A, Lauvaux T, Miles NL, Richardson SJ, Sarmiento DP, Gurney KR, Hardesty RM, Bonin TA, Brewer WA et al (2017) The indianapolis flux experiment (influx): a test-bed for developing urban greenhouse gas emission measurements. Elem Sci Anth 5:21
Dyer A, Hicks B (1970) Flux-gradient relationships in the constant flux layer. Q J R Meteorol Soc 96(410):715–721
Feigenwinter C, Bernhofer C, Eichelmann U, Heinesch B, Hertel M, Janous D, Kolle O, Lagergren F, Lindroth A, Minerbi S et al (2008) Comparison of horizontal and vertical advective CO_2 fluxes at three forest sites. Agric For Meteorol 148(1):12–24
Feigenwinter C, Montagnani L, Aubinet M (2010) Plot-scale vertical and horizontal transport of CO_2 modified by a persistent slope wind system in and above an Alpine forest. Agric For Meteorol 150(5):665–673
Foken T, Wichura B (1996) Tools for quality assessment of surface-based flux measurements. Agric For Meteorol 78(1–2):83–105
Freundorfer A, Rehberg I, Law BE, Thomas C (2019) Forest wind regimes and their implications on cross-canopy coupling. Agric For Meteorol 279(107):696
Ghannam K, Duman T, Salesky ST, Chamecki M, Katul G (2017) The non-local character of turbulence asymmetry in the convective atmospheric boundary layer. Q J R Meteorol Soc 143(702):494–507
Grimmond S, Ward HC (2021) Urban measurements and their interpretation. In: Springer handbook of atmospheric measurements, pp 1391–1423, Springer, Berlin
Jocher G, Marshall J, Nilsson MB, Linder S, De Simon G, Hörnlund T, Lundmark T, Näsholm T, Ottosson Löfvenius M, Tarvainen L et al (2018) Impact of canopy decoupling and subcanopy advection on the annual carbon balance of a boreal scots pine forest as derived from eddy covariance. J Geophys Res Biogeosci 123(2):303–325
Jocher G, Fischer M, Šigut L, Pavelka M, Sedlák P, Katul G (2020) Assessing decoupling of above and below canopy air masses at a Norway spruce stand in complex terrain. Agric For Meteorol 294(108):149
Kaimal JC, Wyngaard JC, Izumi Y, Coté OR (1972) Spectral characteristics of surface-layer turbulence. Q. J. R. Meteorol. Soc 98(417):563–589. https://doi.org/10.1002/qj.49709841707
Kastner-Klein P, Rotach MW (2004) Mean flow and turbulence characteristics in an urban roughness sublayer. Boundary-Layer Meteorol 111:55–84
Katul G, Hsieh CI, Kuhn G, Ellsworth D, Nie D (1997) Turbulent eddy motion at the forest-atmosphere interface. J Geophys Res Atmos 102(D12):13409–13421
Katul G, Peltola O, Grönholm T, Launiainen S, Mammarella I, Vesala T (2018) Ejective and sweeping motions above a peatland and their role in relaxed-eddy-accumulation measurements and turbulent transport modelling. Boundary-Layer Meteorol 169(2):163–184
Katul GG, Banerjee T, Cava D, Germano M, Porporato A (2016) Generalized logarithmic scaling for high-order moments of the longitudinal velocity component explained by the random sweeping decorrelation hypothesis. Phys Fluids 28(9)
Lan C, Liu H, Li D, Katul GG, Finn D (2018) Distinct turbulence structures in stably stratified boundary layers with weak and strong surface shear. J Geophys Res Atmos 123(15):7839–7854
Lan C, Mauder M, Stagakis S, Loubet B, D'onofrio C, Metzger S, Durden D, Herig-Coimbra PH (2024) Intercomparison of eddy-covariance software for urban tall-tower sites. Atmos Meas Tech 17(9):2649–2669
Li D (2019) Turbulent Prandtl number in the atmospheric boundary layer-where are we now? Atmos Res 216:86–105
Lietzke B, Vogt R (2013) Variability of CO_2 concentrations and fluxes in and above an urban street canyon. Atmos Environ 74:60–72
Lin JC, Mitchell L, Crosman E, Mendoza DL, Buchert M, Bares R, Fasoli B, Bowling DR, Pataki D, Catharine D et al (2018) CO_2 and carbon emissions from cities: linkages to air quality, socioeconomic activity, and stakeholders in the Salt Lake city urban area. Bull Am Meteor Soc 99(11):2325–2339
Mahrt L, Thomas CK, Grachev AA, Persson POG (2018) Near-surface vertical flux divergence in the stable boundary layer. Boundary-Layer Meteorol 169:373–393
Matthews B, Schume H (2022) Tall tower eddy covariance measurements of CO_2 fluxes in Vienna, Austria. Atmos Environ 274(118):941

Mauder M, Cuntz M, Drüe C, Graf A, Rebmann C, Schmid HP, Schmidt M, Steinbrecher R (2013) A strategy for quality and uncertainty assessment of long-term eddy-covariance measurements. Agric For Meteorol 169:122–135

Mauder M, Foken T, Aubinet M, Ibrom A (2021) Eddy-covariance measurements. In: Springer handbook of atmospheric measurements, pp 1473–1504, Springer, Berlin

Metzger S (2018) Surface-atmosphere exchange in a box: making the control volume a suitable representation for in-situ observations. Agric For Meteorol 255:68–80

Metzger S, Junkermann W, Mauder M, Butterbach-Bahl K, Trancóny Widemann B, Neidl F, Schäfer K, Wieneke S, Zheng X, Schmid HP et al (2013) Spatially explicit regionalization of airborne flux measurements using environmental response functions. Biogeosciences 10(4):2193–2217

Monin A, Obukhov A (1954) Basic laws of turbulent mixing in the ground surface layer. Tr Geophiz Inst Akad Nauk SSSR 151:163–187

Montagnani L, Grunwald T, Kowalski A, Mammarella I, Merbold L, Metzger S, Sedlák P, Siebicke L (2018) Estimating the storage term in eddy covariance measurements: the ICOS methodology. Int Agrophys 32(4):551–567

Nagano Y, Tagawa M (1995) Coherent motions and heat transfer in a wall turbulent shear flow. J Fluid Mech 305:127–157

Nicolini G, Aubinet M, Feigenwinter C, Heinesch B, Lindroth A, Mamadou O, Moderow U, Mölder M, Montagnani L, Rebmann C et al (2018) Impact of CO_2 storage flux sampling uncertainty on net ecosystem exchange measured by eddy covariance. Agric For Meteorol 248:228–239

Nieuwstadt FT (1984) The turbulent structure of the stable, nocturnal boundary layer. J Atmos Sci 41(14):2202–2216

Oke TR, Mills G, Christen A, Voogt JA (2017) Urban climates. Cambridge University Press, Cambridge

Oliveira PE, Acevedo OC, Sörgel M, Tsokankunku A, Wolff S, Araújo AC, Souza RA, Sá MO, Manzi AO, Andreae MO (2018) Nighttime wind and scalar variability within and above an Amazonian canopy. Atmos Chem Phys 18(5):3083–3099

Panofsky HA, Tennekes H, Lenschow DH, Wyngaard J (1977) The characteristics of turbulent velocity components in the surface layer under convective conditions. Boundary-Layer Meteorol 11:355–361

Peltola O, Lapo K, Thomas C (2021) A physics-based universal indicator for vertical decoupling and mixing across canopies architectures and dynamic stabilities. Geophys Res Lett 48(5):e2020GL091615

Raupach M, Thom AS (1981) Turbulence in and above plant canopies. Annu Rev Fluid Mech 13(1):97–129

Roth M, Jansson C, Velasco E (2017) Multi-year energy balance and carbon dioxide fluxes over a residential neighbourhood in a tropical city. Int J Climatol 37(5):2679–2698

Rotta J (1951) Statistical theory of inhomogeneous turbulence. Z Phys 129:257–572

Sabbatini S, Mammarella I, Arriga N, Fratini G, Graf A, Hörtnagl L, Ibrom A, Longdoz B, Mauder M, Merbold L et al (2018) Eddy covariance raw data processing for CO_2 and energy fluxes calculation at ICOS ecosystem stations. Int Agrophys 32(4):495–515

Schmutz M, Vogt R (2019) Flux similarity and turbulent transport of momentum, heat and carbon dioxide in the urban boundary layer. Boundary-Layer Meteorol 172:45–65

Schmutz M, Vogt R, Feigenwinter C, Parlow E (2016) Ten years of eddy covariance measurements in Basel, Switzerland: seasonal and interannual variabilities of urban CO_2 mole fraction and flux. J Geophys Res Atmos 121(14):8649–8667

Siebicke L, Hunner M, Foken T (2012) Aspects of CO_2 advection measurements. Theoret Appl Climatol 109(1):109–131

Stagakis S, Chrysoulakis N, Spyridakis N, Feigenwinter C, Vogt R (2019) Eddy covariance measurements and source partitioning of CO_2 emissions in an urban environment: application for Heraklion, Greece. Atmos Environ 201:278–292

Stiegler C, June T, Markwitz C, Camarretta N, Ali AA, Knohl A (2023) Wind regimes above and below a dense oil palm canopy: detection of decoupling and its implications on CO_2 flux estimates. Agric For Meteorol 341(109):668

Stull RB (2012) An introduction to boundary layer meteorology, vol 13. Springer Science & Business Media, Berlin

Sun J, Mahrt L, Banta RM, Pichugina YL (2012) Turbulence regimes and turbulence intermittency in the stable boundary layer during cases-99. J Atmos Sci 69(1):338–351

Sun J, Lenschow DH, LeMone MA, Mahrt L (2016) The role of large-coherent-eddy transport in the atmospheric surface layer based on cases-99 observations. Boundary-Layer Meteorol 160:83–111

Sun J, Takle ES, Acevedo OC (2020) Understanding physical processes represented by the Monin–Obukhov bulk formula for momentum transfer. Boundary-Layer Meteorol 177(1):69–95

Thomas CK, Martin JG, Law BE, Davis K (2013) Toward biologically meaningful net carbon exchange estimates for tall, dense canopies: multi-level eddy covariance observations and canopy coupling regimes in a mature Douglas-fir forest in Oregon. Agric For Meteorol 173:14–27

Wang L, Li D, Gao Z, Sun T, Guo X, Bou-Zeid E (2014) Turbulent transport of momentum and scalars above an urban canopy. Boundary-Layer Meteorol 150:485–511

Wang Y, Wang B, Lan C, Fang R, Zheng B, Lu J, Zheng D (2022) Improved quadrant analysis for large-scale events detection in turbulent transport. Atmosphere 13(3):489

Ward H, Evans JG, Grimmond CSB (2013) Multi-season eddy covariance observations of energy, water and carbon fluxes over a suburban area in Swindon, UK. Atmos Chem Phys 13(9):4645–4666

Ward HC, Rotach MW, Gohm A, Graus M, Karl T, Haid M, Umek L, Muschinski T (2022) Energy and mass exchange at an urban site in mountainous terrain-the Alpine city of innsbruck. Atmos Chem Phys 22(10):6559–6593

Xu K, Metzger S, Desai AR (2017) Upscaling tower-observed turbulent exchange at fine spatio-temporal resolution using environmental response functions. Agric For Meteorol 232:10–22

Xu K, Metzger S, Desai AR (2018) Surface-atmosphere exchange in a box: space-time resolved storage and net vertical fluxes from tower-based eddy covariance. Agric For Meteorol 255:81–91